

High-Performing Monometallic Cobalt Layered Double Hydroxide Supercapacitor with Defined Local Structure

Pierre Vialat, Christine Mousty, Christine Taviot-Gueho, Guillaume Renaudin, Herve Martinez, Jean-Charles Dupin, Erik Elkaim, and Fabrice Leroux*

Through a topochemical oxidative reaction (TOR) under air, a β -Co(OH)₂ brucite type structure is converted into a monometallic Co^{II}Co^{III}-CO₃ layered double hydroxide (LDH). The structural and morphological characterizations are performed using powder X-ray diffraction, Fourier-transformed IR spectroscopy, and scanning and transmission electron microscopy. The local structure is scrutinized using an extended X-ray absorption fine structure, X-ray absorption near-edge structure, and pair distribution function analysis. The chemical composition of pristine material and its derivatives (electrochemically treated) are identified by thermogravimetry analysis for the bulk and X-ray photoelectron spectroscopy for the surface. The electrochemical behavior is investigated on deposited thin films in aqueous electrolyte (KOH) by cyclic voltammetry and electrochemical impedance spectroscopy, and their capacitive properties are further investigated by Galvanostatic cycling with potential limitation. The charge capacity is found to be as high as 1490 F g⁻¹ for Co^{II}Co^{III}-CO₃ LDH at a current density of 0.5 A g⁻¹. The performances of these materials are described using Ragone plots, which finally allow us to propose them as promising supercapacitor materials. A surface-to-bulk comparison using the above characterization techniques gives insight into the cyclability and reversibility limits of this material.

1. Introduction

Complementary to lithium or lithium-ion batteries that provide high specific energy, electrochemical capacitors—so-called “supercapacitors”—have the potential to deliver a high power density in a very short time and excellent cyclability, thus explaining the renewed interest for such electrochemical devices in different domains such as digital telecommunication

systems, uninterruptible power supplies for computers, and electric/hybrid vehicles. Supercapacitors can be divided into two types according to the mechanisms involved in energy storage: (i) superficial, electrochemical double-layer capacitors (EDLCs), as illustrated by carbon materials,^[1] or (ii) multielectron-transfer faradaic reaction, with fast charge discharge properties: “pseudo-capacitors” or redox capacitors, as exemplified by some metal oxides.^[2,3]

Materials with large surface areas and/or open structures are extensively investigated for application as supercapacitors. Regarding high performance, layered double hydroxide (LDH) phases containing electroactive species have been reported to exhibit very large pseudocapacitive properties. Briefly, LDH materials are intercalation compounds represented by the general formula $[M^{II}_{1-a}M^{III}_a(OH)_2]^{x+} [(A^{n-})_{a/n}]_y \cdot y H_2O$ (abbreviated as M^{II}M^{III}-A), where M^{II} is a divalent metal cation or a mixture of divalent cations and M^{III} is a trivalent

metal. Aⁿ⁻ is the interlayer anion compensating the positive charge of the metal hydroxide layers. Significantly high performances have been obtained for CoNiAl-LDH with capacitances as high as 960 F.g⁻¹^[4] as well as for Co₂Al-NO₃ with capacitances of 833 and 466 F.g⁻¹.^[5,6] Since LDHs usually suffer from a lack of electronic conductivity, composites of graphite and CoAl-LDH assembled to yield graphene nanosheets with embedded LDH platelets have been prepared to optimize the capacitance, and values as high as 711.5 and 772 F.g⁻¹ have been reported at a current density of 1 A.g⁻¹,^[7,8] as well as the use of graphene oxide layers, resulting in a capacitance of 1031 F.g⁻¹ at 1 A.g⁻¹.^[9]

In the present study, we combine the properties of layered materials with the electronic conductivity provided by the association of Co^{II}/Co^{III} electroactive cations into a LDH hydroxide layer. The material was prepared through a topochemical oxidative reaction (TOR), resulting in the partial cobalt cation oxidation from an oxidation state of +2 to +3. As previously reported,^[10–13] brucite-like cobalt hydroxide Co(OH)₂ converts under air to a Co^{II}Co^{III}-CO₃ LDH phase, but the associated electrochemical properties of such a material have never been studied, and its local structure has not been uncovered.

P. Vialat, Prof. C. Mousty, Prof. C. Taviot-Gueho,
Prof. G. Renaudin, Prof. F. Leroux
Clermont Université
Université Blaise Pascal
Institut de Chimie de Clermont-Ferrand
UMR-CNRS 6296 F-63000, CLERMONT-FERRAND, France
E-mail: Fabrice.Leroux@univ-bpclermont.fr
Prof. H. Martinez, Dr. J.-C. Dupin
Université de Pau et des Pays de l'Adour
UMR5254 – IPREM, F-64053 Pau Cedex 09, France
Dr. E. Elkaim
Synchrotron SOLEIL, L'Orme des Merisiers
BP 48 91192, Saint-Aubin, France



DOI: 10.1002/adfm.201400310

The Co^{III} surface composition, determined using X-ray photoelectron spectroscopy (XPS), may be compared to the bulk composition by coupling thermogravimetric analysis (TGA) and iodometric titration of the Co^{III} species along with other characterizations described below. All the solids were then fully characterized by X-ray diffraction (XRD) and the local structure was unravelled using extended X-ray absorption fine structure (EXAFS), X-ray absorption near-edge structure (XANES), and pair distribution function (PDF) analyses. The particle morphology was observed with scanning and transmission electron microscopy (SEM and TEM). The electrochemical characteristics were evaluated by cyclic voltammetry (CV) and electrochemical impedance spectroscopy (EIS) on thin LDH films. The capacitive properties were finally determined using Galvanostatic cycling with potential limitation (GCPL) analysis at different current densities to map the power–energy dependence in a Ragone diagram.

2. Results and Discussion

2.1. Chemical and Structural Characterizations of $\text{Co}^{\text{II}}\text{Co}^{\text{III}}\text{-CO}_3$

Adapting the protocol described by Xu and Zeng^[13] using air as the oxidizing agent (TOR reaction) of $\text{Co}(\text{NO}_3)_2$ in the precipitation process, a mixed oxidation state cobalt (Co^{II} and Co^{III}) hydroxide compound was prepared.

In Figure 1A, the powder X-ray diffraction pattern of a $\text{Co}^{\text{II}}\text{Co}^{\text{III}}\text{-CO}_3$ sample obtained by TOR reaction is compared to that of a $\text{Co}_2\text{Al-CO}_3$ reference sample, indicating the formation of a layered double hydroxide phase with three distinct regions: (1) the low angle region ($<30^\circ$ 2θ) containing the basal reflections (00 l), which positions depend on the size of the intercalated anion; (2) the high angle region ($>55^\circ$ 2θ) containing the ($hk0$) and (hkl) reflections characteristic of the metal hydroxide layers; (3) the mid- 2θ region ($30\text{--}55^\circ$ 2θ), containing the ($h0l$) and ($0kl$) reflections, which positions depend on the polytype.

The powder XRD (PXRD) pattern of $\text{Co}_2\text{Al-CO}_3$ is typical of a stacking disorder with a very pronounced asymmetric broadening of the ($h0l$)/(0 kl) reflections in the mid- 2θ region, also called the Warren fall, while the (00 l) and (110)/(113) reflections are not affected.^[14] Small crystallite size effects are likely to be responsible for the overall broadening of the Bragg reflections in the PXRD patterns of $\text{Co}^{\text{II}}\text{Co}^{\text{III}}\text{-CO}_3$.

Owing to the very diffuse mid- 2θ region of $\text{Co}_2\text{Al-CO}_3$, the cell parameters a and c were determined from single-peak profile analyses of the (00 l) and (110) reflections, respectively, using a pseudo-Voigt peak shape and assuming the R-3 m space group: $a = 2\sqrt{3}d_{110} = 3.063(2)$ Å, $c = 3\sqrt{3}d_{003} = 22.63(2)$ Å, and $d_{003} = 7.54$ Å. Furthermore, the size of the coherent domains was estimated from the full width at half-maximum (FWHM) of the (00 l) and (110) reflections, both unaffected by the structural disorder and using the Scherrer formula.^[15] The dimensions thus calculated are $L_{00l} = 32.5$ nm and $L_{110} = 50.0$ nm, respectively, in agreement with the platelet shape of LDH particles, i.e., a thickness L_{00l} much lower than the in-plane L_{110} dimension.

For the $\text{Co}^{\text{II}}\text{Co}^{\text{III}}\text{-CO}_3$ sample, the unit cell parameters were determined from the Le Bail method (pattern matching): $a = 3.0468(9)$ Å, $c = 22.66(1)$ Å. The resulting interlayer distance

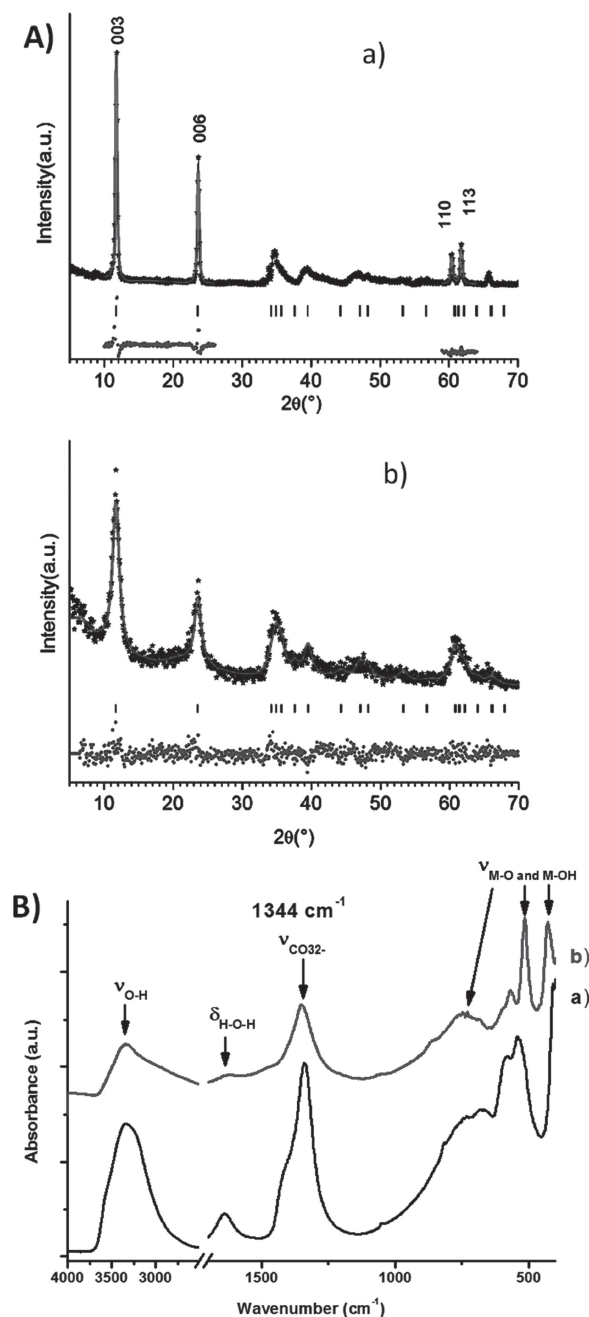


Figure 1. A) X-ray powder diffraction data ($\lambda = 1.5418$ Å) for a) $\text{Co}_2\text{Al-CO}_3$ and b) $\text{Co}^{\text{II}}\text{Co}^{\text{III}}\text{-CO}_3$. Results of the profile match the R-3 m space group: experimental X-ray powder diffraction patterns (dots), calculated data (continuous line), Bragg reflections (ticks), and difference profile. B) FTIR spectra of a) $\text{Co}_2\text{Al-CO}_3$, and b) $\text{Co}^{\text{II}}\text{Co}^{\text{III}}\text{-CO}_3$.

$d_{003} = 7.55$ Å is identical to that observed for $\text{Co}_2\text{Al-CO}_3$, thus confirming the presence of carbonate anions^[16] in the interlayer space to compensate the positive charge created by the oxidation of Co^{II} within the hydroxide layers (Table 1). It is worth noting that the implementation of corrections for anisotropic size broadening was essential to reach acceptable reliability factors for the pattern-matching analysis. The modeling of the Lorentzian part of the peak broadening with linear combinations

Table 1. Cell parameters and sizes of the coherent domains determined from X-ray diffraction (numbers in parenthesis are given for accuracy on the last number).

| Compound | Cell parameter <i>a</i> [Å] | Cell parameter <i>c</i> [Å] | Interlayer distance [Å] | <i>L</i> ₀₀₁ [Å] | <i>L</i> ₁₁₀ [Å] |
|---|--------------------------------|--------------------------------|----------------------------|--------------------------------|--------------------------------|
| Co ₂ Al-CO ₃ | 3.063 (2) | 22.63 (2) | 7.54 | 325 | 500 |
| Co ^{II} Co ^{III} -CO ₃ | 3.0468 (9) | 22.66 (1) | 7.55 | 45 | 53 |

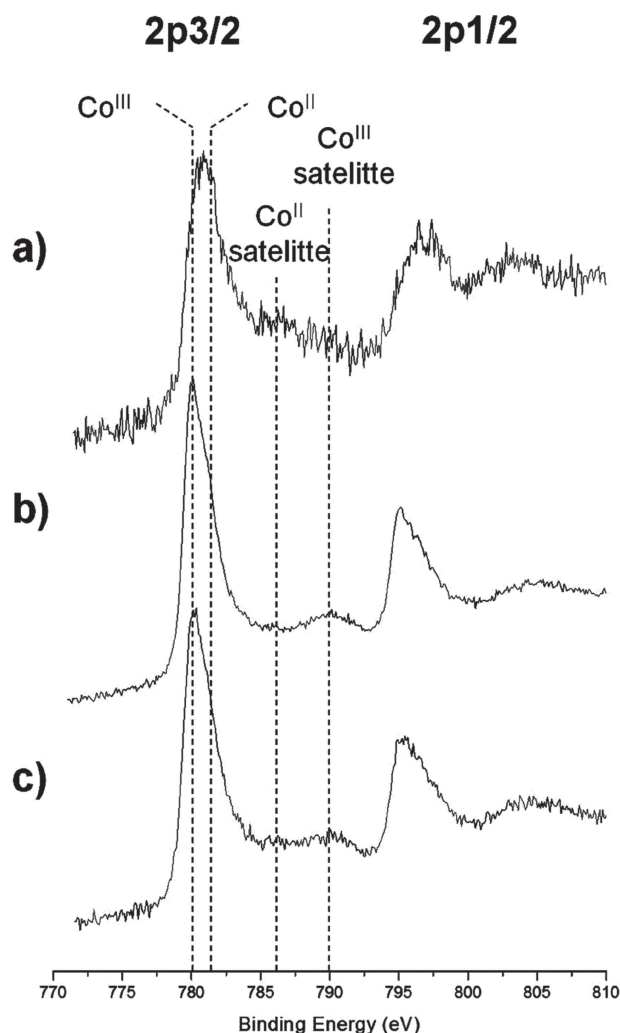
of spherical harmonics allowed the calculation of the average apparent sizes in the directions corresponding to a given Bragg reflection.^[17] The values thus obtained along the [110] and [001] directions are *L*₁₁₀ = 5.3 nm and *L*₀₀₁ = 4.5 nm, respectively. Therefore, the dimensions of the coherent domains are ten times smaller than for Co₂Al-CO₃, in agreement with the lower crystallinity of Co^{II}Co^{III}-CO₃.

Fourier-transformed IR (FTIR) spectra (Figure 1B) confirm the formation of a hydroxylated structure, similar to that of Co₂Al-CO₃ LDH. Indeed, all the characteristic bands of brucite-like metal hydroxide layers are observed: the vibration band of the O-H bonds around 3500 cm⁻¹, an H₂O vibration band at 1600 cm⁻¹, and M-O/M-OH bands above 1000 cm⁻¹. The carbonate antisymmetric stretching vibration *v*₃ appears at 1344 cm⁻¹. Well defined vibration bands around 400–500 cm⁻¹, characteristic of a well-ordered intralayer arrangement,^[18] have to be correlated with PDF analysis.

To determine the bulk composition of Co^{II}Co^{III}-CO₃, in particular the Co^{III}/Co_{tot} molar ratio, the total amount of cobalt (Co_{tot} = Co^{II} + Co^{III}) in the sample was determined by TGA analysis while the Co^{III} content was obtained by iodometric titration. The Co^{III}/Co_{tot} molar ratio was found to be 0.12 ± 0.02, which is surprisingly low; LDH materials obtained by a coprecipitation technique generally display M^{II}/M^{III} ratios ranging between 2 and 4. To go further in the knowledge of electronic changes at the surface of materials, XPS was used as a fine probe (Table 2) in the case of pristine and electrochemically treated LDH (see also Section 2.3.4), to give a highly resolved overview of the chemical composition, although investigated over the very first layers of the materials (5 nm depth analysis). The fitting of well-defined Co 2p_{3/2} peaks for the pristine material (Figure 2a) clearly highlights the coexistence of two oxidation states for cobalt, with a Co^{III} component at 780.0 ± 0.1 eV (with an associated satellite structure at 789.8 ± 0.1 eV) and a Co^{II} component at 781.2 ± 0.1 eV (satellite structure at 785.7 ± 0.2 eV). These attributions were possible using Co₃O₄ spinel and Co₂Al-CO₃ LDH containing defined amount of Co^{III} as standards. For the Co^{II}Co^{III}-CO₃ LDH, the Co^{III}/Co_{tot} ratio calculated from the Co2p spectrum deconvolution was found to be 0.15, a value very close to that determined above from iodometric titration, although slightly higher. This small difference can be attrib-

Table 2. XPS, PDF, and iodometric titration determinations of Co^{III} and Co^{II} contents before and after electrochemical treatment.

| Sample | XPS | | PDF | | I ₂ Titration | |
|--|--------------------|---------------------|--------------------|---------------------|--------------------------|---------------------|
| | % Co ^{II} | % Co ^{III} | % Co ^{II} | % Co ^{III} | % Co ^{II} | % Co ^{III} |
| Co ^{II} Co ^{III} -CO ₃ | 85 | 15 | 89 | 11 | 88 | 12 |
| Co ^{II} Co ^{III} -CO ₃ ox | 31 | 69 | 46 | 54 | 41 | 59 |
| Co ^{II} Co ^{III} -CO ₃ ox/red | 55 | 45 | 79 | 21 | 66 | 34 |

**Figure 2.** Co_{2p} XPS spectra of a) Co^{II}Co^{III}-CO₃, b) Co^{II}Co^{III}-CO₃ oxidized at 0.45 V/SCE, and c) Co^{II}Co^{III}-CO₃ oxidized at 0.45 V/SCE and then reduced at 0.0 V/SCE.

uted to the fact that XPS is mainly a surface analysis, while iodometric titration concerns the bulk. Hence, the surface chemical composition as determined by XPS is Co^{II}_{0.85}Co^{III}_{0.15}(OH)₂(CO₃)_{0.07}•0.9 H₂O while the bulk chemical formula is Co^{II}_{0.88}Co^{III}_{0.12}(OH)₂(CO₃)_{0.06}•0.9 H₂O, obtained from I₂ titration. These results suggest that only 1/7 of the Co^{II} sites within the hydroxide layers are oxidized to Co^{III} using TOR.

Co K absorption near-edge spectra (XANES) for Co^{II}Co^{III}-CO₃ are displayed with Co₂Al-CO₃ LDH and Co₃O₄ reference products (Figure 3A). It is known that edge absorption features are sensitive to the site environment, i.e., coordination number and metal oxidation state.^[19] Three distinct edge

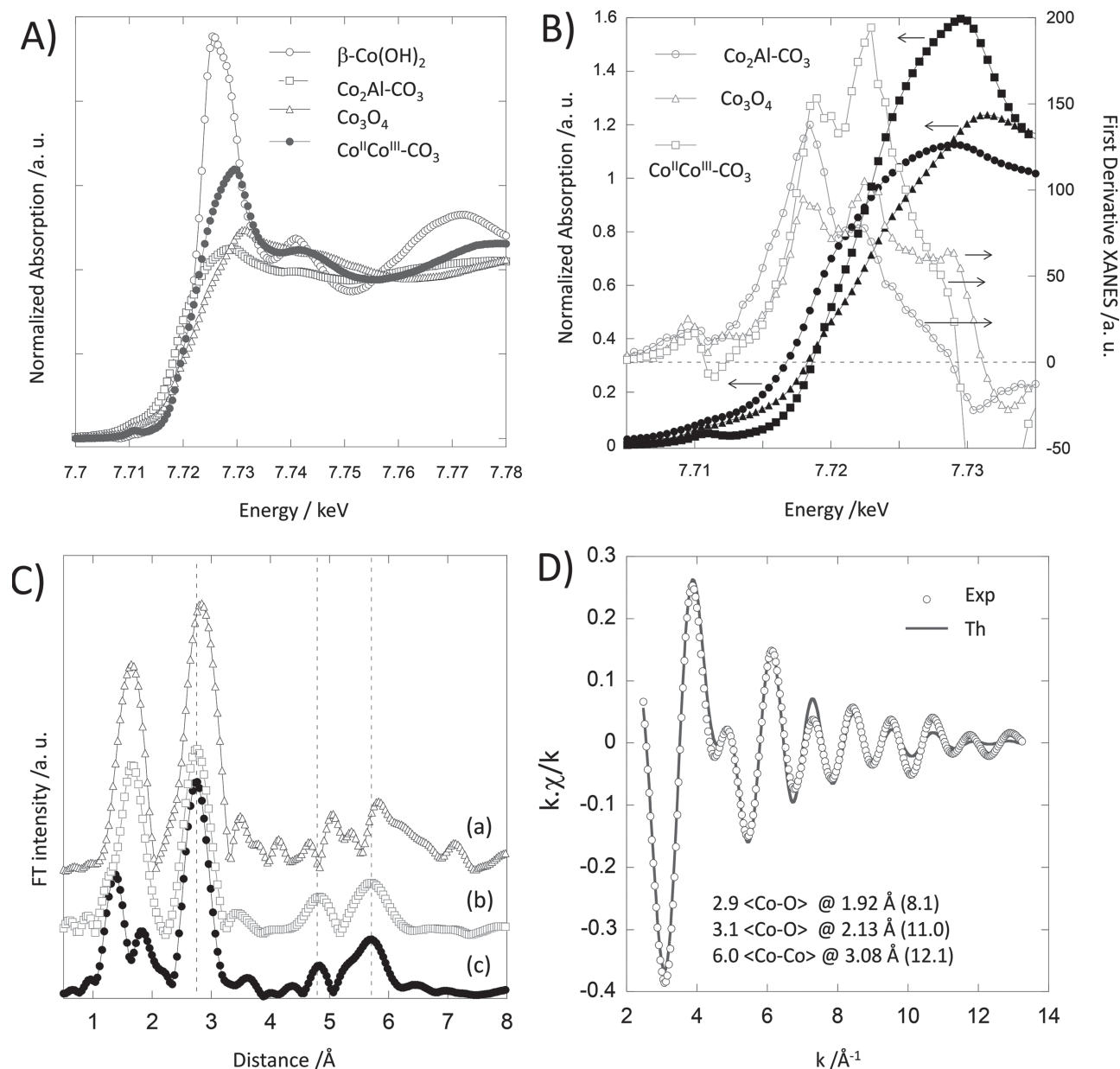


Figure 3. Co K-edge XANES A) first derivative and B) spectra of the Co^{II}/Co^{III}-CO₃ sample compared to references. C) Comparison of the Co K-edge Fourier transform magnitudes of k^3 -weighted EXAFS spectra for a) β -Co(OH)₂, b) Co₂Al-CO₃ LDH, and c) Co^{II}/Co^{III}-CO₃ (note that the distances are not corrected from phase shift). Cation correlations at $\sqrt{3}a$, and $2a$ are visualized by dashed lines. D) $k^3(k)$ refinement curves for the sample after air oxidation including the two first ligand spheres <Co-O> and <Co-Co> (Debye-Waller σ^2 (10⁻³·Å²) factors are indicated in parenthesis).

features are observed. The weak absorption pre-edge peaks are associated with the dipole-forbidden $1s \rightarrow 3d$ electronic transitions, partially allowed in the case of the $3d$ and $4p$ orbitals mixing. Note that such hybridization is generally observed for non-centro-symmetric environments for oxygen atoms in the first metal coordination sphere. Indeed, the transition metals in tetrahedral sites usually show much more intense pre-edge peaks than when located in octahedral sites due to a decrease in the inversion center in the tetrahedral coordination symmetry. The strong main absorption peak is a dipole-allowed $1s \rightarrow 4p$ transition, and the associated energy position is considered to evaluate an average oxidation state (vide infra). The shoulder

corresponds to the electronic dipole-allowed transition of a $1s$ core electron to an unoccupied $4p$ bound state, which is modified by the ligand-to-metal charge transfer, also called a “shake-down” process.^[20]

For Co^{II}/Co^{III}-CO₃, the associated pre-edge of low intensity indicates that Co atoms are located in Oh-type sites. The presence of tetrahedrally coordinated Co atoms even in small relative numbers is usually depicted as for β -type cobalt hydroxide, where 1/5 to 1/6 of the Co^{II} at octahedral sites are replaced by pairs of tetrahedrally coordinated Co^{II}.^[21] Since the pre-edge is very sensitive to deviation in coordination and its associated intensity is similar to brucite, it discards here the possibility

of forming Co in tetrahedral coordination that would have explained shorter distances in terms of bond length and valence, as discussed below.^[22] On the other hand, one can note that the energy threshold is sensitive to the oxidation state, leading to a shift of the 1s to 4p transition to higher energy with an increase of the valence. Indeed, the core electrons being more strongly held to the nucleus, their photo-ionization necessitates higher photon energies and such a shift is often associated with a “chemical shift”. This appears to be the case for $\text{Co}^{\text{II}}\text{Co}^{\text{III}}\text{-CO}_3$, since the main edge is shifted toward a higher energy when compared to either $\beta\text{-Co(OH)}_2$ or $\text{Co}_2\text{Al-CO}_3$. Discrete features visualized on the first derivative XANES curve versus energy help to measure the precise position in energy of the hump-shaped absorption process. The position in energy is taken when the first XANES derivative is equal to zero at around 7.73 keV (Figure 3B). Interestingly, one notes that by changing the type of ligand (i.e. hydroxyl for oxygen), the energy position is slightly shifted in agreement with the bond length variation, as observed between $\beta\text{-Co(OH)}_2$ versus CoO (data not shown).

Pre-edge and edge XANES peaks inform us about the Co cation coordination remaining in octahedral environments with an average oxidation state increased by +2 to 2.15, yielding a composition $\text{Co}^{\text{II}}_{0.85}\text{Co}^{\text{III}}_{0.15}$, which agrees well with the above characterizations. The accommodation of Co^{III} into the hydroxide layers of the LDH has already been investigated by means of X-ray absorption spectroscopy (XAS) in the case of low layer charge Co_5Al LDH, uncovering a partial oxidation of Co^{II} to Co^{III} .^[23]

EXAFS oscillations were analyzed to identify the local structural variations around Co sites in $\text{Co}^{\text{II}}\text{Co}^{\text{III}}\text{-CO}_3$. Fourier transform of k^3 -weighted EXAFS spectra are displayed in Figure 3C. FT spectra were not phase-corrected, explaining why the R-values are shorter. We attribute the first peaks between 1.0 and 2.0 Å and the second peak at approximately 2.5 Å to, respectively, the single scattering paths of the closest oxygen (i.e. M-O) and the second neighboring transition metals within the same a-b plane (i.e. M-M) surrounding the Co absorbing atoms. These two contributions were refined, resulting in the presence of oxygen atoms at two distances 1.92 and 2.13 Å and a first metal-metal distance at 3.08 Å, as shown in the inset text of Figure 3D. These results are consistent with values reported elsewhere for $\text{Co}^{\text{II}}\text{-O}_{\text{OH}}$ bonds for octahedrally coordinated Co^{II} , which are around 2.0 to 2.1 Å^[21,24–28] and $\text{Co}^{\text{III}}\text{-O}_{\text{OH}}$ bounds for octahedrally coordinated Co^{III} , which are close to 1.9 Å.^[26,29,30] By applying a simple bond-valence parameters concept, an average oxidation state close to 2.5 is observed. We tentatively ascribe this slight discrepancy to an inaccuracy in the neighbor's number between short and long Co-O distances, probably overestimating the shorter one due to noise in the short k -value Fourier transform (experiments performed at room temperature).

At larger R-values, the Fourier transform of the $\text{Co}^{\text{II}}\text{Co}^{\text{III}}\text{-CO}_3$ sample is quite similar to $\text{Co}_2\text{Al-CO}_3$, with the observation of a cation-cation correlation at a distance of a , $\sqrt{3}a$, and $2a$ (Figure 3C), characteristic of the LDH intralayer cation local arrangement, and slightly different from $\beta\text{-Co(OH)}_2$. This indicates that the average arrangement of Co cations in the ab-plane is similar between LDH-type compounds in spite of the ionic radius difference between Al^{III} (51 pm) and Co^{III} (63 pm),

and also that it does not adopt the in-plane organization of the $\beta\text{-Co(OH)}_2$ phase that presents edge-sharing $\text{Co}^{\text{II}}(\text{OH})_6$ octahedra of similar sizes. It further confirms that the air oxidation is a topochemical reaction occurring at the local scale converting $\beta\text{-Co(OH)}_2$ into an LDH-type compound.

To further explore the cation distribution within the hydroxide layers, the approach of atomic pair distribution function analysis was used. The PDF obtained for the $\text{Co}^{\text{II}}\text{Co}^{\text{III}}\text{-CO}_3$ sample presented Figure 4 is quite similar to that recently published by Taviot-Gueho et al.^[14,31] for other related LDH compounds. Consistent with the crystalline character of this material, the oscillations of the PDFs extend over 50 Å (see the Supporting Information). For r values below the interlayer distance d_{003} , the first peak with a large maximum centered at $r \sim 1.97$ Å is attributed to the nearest-neighbor Co-O_{OH} correlation, while the Co-Co correlations contribute to the peaks observed at a (~ 3.07 Å), $\sqrt{3}a$ (~ 5.33 Å), and $2a$ (~ 6.14 Å); the other peaks are the result of multiple pairs.

Besides the identification of low- r peak positions, it is also possible to reveal details about the local distortions and number of neighboring atoms by extracting the PDF peak width and area. Hence when the feature of the first peak corresponding to the closest O_{OH} shell around $\text{Co}^{\text{II}}/\text{Co}^{\text{III}}$ atoms is scrutinized, a left shoulder is also observed. It implies that the first contribution can be modeled by the superposition of two components (Figure 4B). By fitting this peak with two Gaussians, two distances are found at 1.92 Å and 2.02 Å, which can be unambiguously attributed to $\text{Co}^{\text{II}}\text{-O}_{\text{OH}}$ and $\text{Co}^{\text{III}}\text{-O}_{\text{OH}}$ bonds, respectively (vide supra). Notwithstanding the difference in oxidation degrees, one can assume that Co^{II} and Co^{III} cations display the same X-ray scattering power and, therefore, the relative percentage of number of mole of Co^{II} and Co^{III} can be determined in a straightforward way from peak areas. The values thus obtained, i.e., 89% of Co^{II} and 11% of Co^{III} , are in agreement with XPS analysis and iodometric titration (Table 2).

2.2. Morphological Characterization

To visualize the texture and morphology of the as-made thin films by SEM, the aqueous suspensions of LDH platelets were deposited onto a platinum substrate. The image obtained with low magnification (Figure 5A) shows a $\text{Co}^{\text{II}}\text{Co}^{\text{III}}\text{-CO}_3$ film homogeneously covering the entire Pt surface. At higher magnification (Figure 5B,C), little aggregated platelets are observed with lateral dimensions ranging from ~ 50 nm to 200 nm and an average size for most of the observed particles of around 100 nm. This is consistent with the poor crystallinity observed by XRD analysis. For $\text{Co}_2\text{Al-CO}_3$, well crystallized hexagonal platelets are observed (Figure 6A,C) with main dimensions around 200–250 nm and well defined sheets with a regular spacing of ~ 1 nm. The average number of stacked sheets is 40 (Figure 6E), a value very close to that deduced from XRD data, i.e., L_{001}/d_{003} ratio = 43 ($32.5/0.754$). Highly aggregated small particles with diameters around 50 nm are observed in case of $\text{Co}^{\text{II}}\text{Co}^{\text{III}}\text{-CO}_3$ (Figure 6B,D). Selective area electronic diffraction (SAED) of the samples once again confirms the difference in crystallinity between both samples; while well defined hexagonal SAED plots are observed for $\text{Co}_2\text{Al-CO}_3$, only circular halos with weak

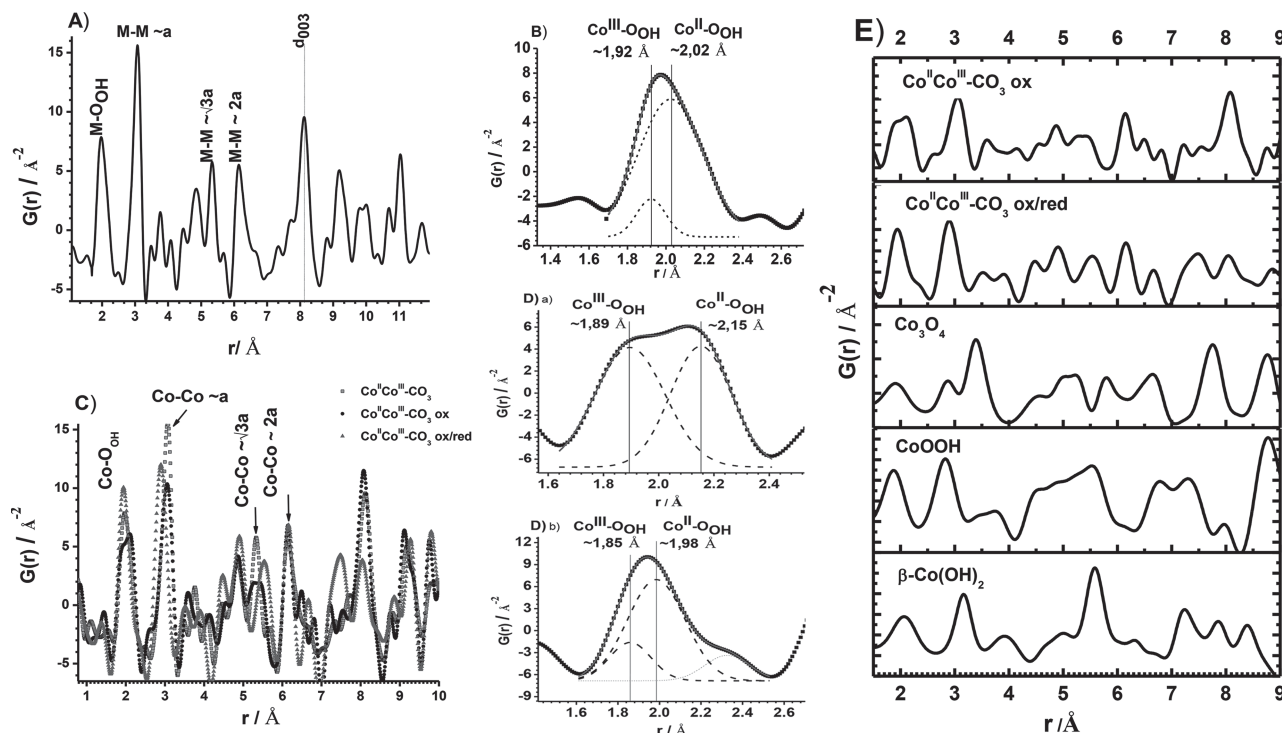


Figure 4. A) Experimental pair distribution function of $\text{Co}^{\text{II}}/\text{Co}^{\text{III}}\text{-CO}_3$; the major contributions are labeled according to Taviot-Gueho et al.^[14] B) Gaussian fit to the first peaks in the PDF: experimental data (black squares), fitted data (solid line), individual Gaussians (dashed lines); peaks are labeled with the corresponding atomic pairs. C) Experimental PDFs of electrochemically treated samples of $\text{Co}^{\text{II}}/\text{Co}^{\text{III}}\text{-CO}_{3\text{ox}}$ (circles) and $\text{Co}^{\text{II}}/\text{Co}^{\text{III}}\text{-CO}_{3\text{ox/red}}$ (triangles) compared to the starting phase (squares). D) Gaussian fit to the first peaks in the PDFs for a) $\text{Co}^{\text{II}}/\text{Co}^{\text{III}}\text{-CO}_{3\text{ox}}$ and b) $\text{Co}^{\text{II}}/\text{Co}^{\text{III}}\text{-CO}_{3\text{ox/red}}$: experimental data (squares), fitted data (solid line), individual Gaussians (dashed lines). Peaks are labeled with the corresponding atomic pairs. E) Experimental PDFs of $\text{Co}^{\text{II}}/\text{Co}^{\text{III}}\text{-CO}_{3\text{ox}}$ and $\text{Co}^{\text{II}}/\text{Co}^{\text{III}}\text{-CO}_{3\text{ox/red}}$ compared to calculated PDFs of Co_3O_4 (ICSD, 9005891), CoOOH (9009449), and $\beta\text{-Co(OH)}_2$ (9009101).

intensity light points (characteristic of quasi amorphous materials) are visualized for $\text{Co}^{\text{II}}/\text{Co}^{\text{III}}\text{-CO}_3$.

2.3. Electrochemical Characterization


2.3.1. Cyclic Voltammetry

$\text{Co}^{\text{II}}/\text{Co}^{\text{III}}\text{-CO}_3$ free of electronic additives characterized by cyclic voltammetry in 0.1 M KOH aqueous electrolyte exhibits a well defined anodic peak at 0.250 V/SCE, associated with a reduction peak at 0.073 V/SCE, leading to a difference of potential (ΔE_p) of 0.177 V (Figure 7A). The number of mole of oxidized (n_{ox}^*) or reduced (n_{red}^*) cobalt cations during a reversible potential sweep is estimated from the oxidation and reduction peak areas measured at a low scan rate (Q_a at $\nu = 5 \text{ mV}\cdot\text{s}^{-1}$). According to the formula and the total amount of LDH coated on the electrode surface, the percentage of electroactive Co^{II} on the electrochemical process may be addressed, i.e., the percentage of Co^{II} cations involved in the electrochemical oxidation process. The obtained percentages are 28% for $\text{Co}^{\text{II}}/\text{Co}^{\text{III}}\text{-CO}_3$ and only 10% for $\text{Co}_2\text{Al-CO}_3$, underlining an electrochemical oxidation of Co^{II} more efficient for the $\text{Co}^{\text{II}}/\text{Co}^{\text{III}}\text{-CO}_3$ structure than for the $\text{Co}_2\text{Al-CO}_3$ LDH. Almost 1/3 of Co^{II} cations present in the $\text{Co}^{\text{II}}/\text{Co}^{\text{III}}\text{-CO}_3$ can be electrochemically oxidized to Co^{III} . Interestingly, the net balance efficiency per cycle $n_{\text{red}}/n_{\text{ox}} < 1$.

2.3.2. Impedance Spectroscopy

To scrutinize the intimate modifications in terms of charge transfer occurring during the sweep process, electrochemical impedance spectroscopy (EIS) measurements were performed after oxidation upon cycling (ten cycles) (OCP_f). EI spectra over a 25 mHz–100 kHz frequency range display quasi-straight lines for both samples (Figure 7B). Impedance data can be fitted using an equivalent circuit model (Table 3), taking into account the representation of pseudo-capacitance and the electrolyte resistance only with two constant-phase components (CPE_{et} and CPE_d) (Table 3). The electrolyte resistance is found here to be constant at around 100 Ω. The phase constants for CPE_{et} corresponding to capacity linked with electronic transfer into the layers were refined between 0.94 and 0.98, corresponding to

Table 3. Equivalent circuit and EI spectra refinement values obtained with ZView software.

| Compound |  | | | | |
|--|--|--|-----------------------------|---|----------------------------|
| | R_{el} [Ω] | CPE_{et} [$10^{-3} \text{ F}^{-1} \text{ s}^{n+1}$] | $n(\text{CPE}_{\text{et}})$ | CPE_{d} [$10^{-2} \text{ F}^{-1} \text{ s}^{n+1}$] | $n(\text{CPE}_{\text{d}})$ |
| $\text{Co}^{\text{II}}/\text{Co}^{\text{III}}\text{-CO}_3$ | 102.3 | 3.27 | 0.94 | 2.63 | 0.50 |
| $\text{Co}_2\text{Al-CO}_3$ | 121.3 | 0.11 | 0.92 | 2.37 | 0.50 |

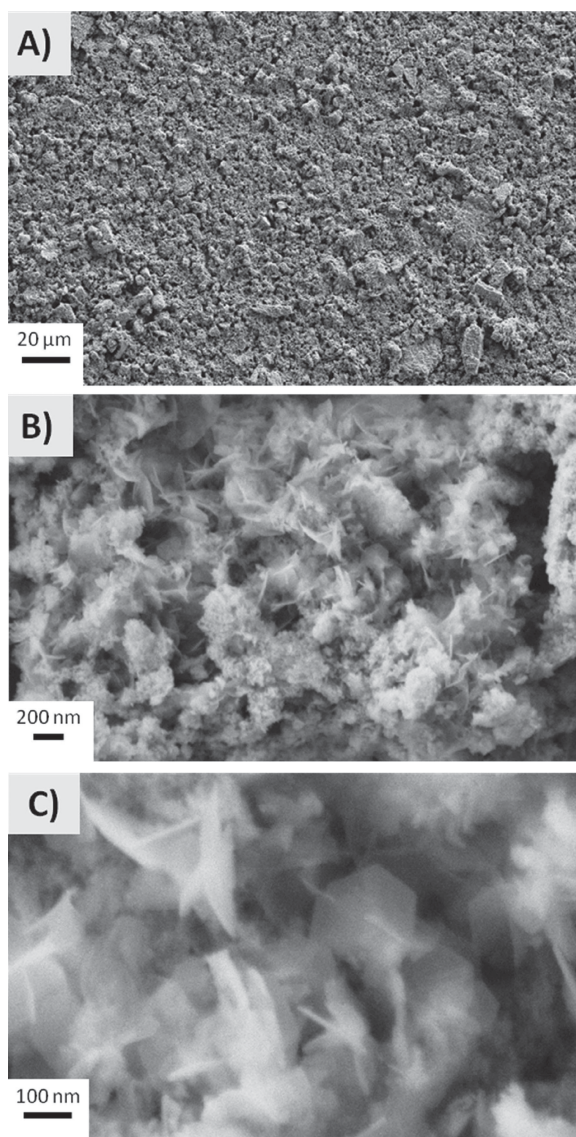


Figure 5. SEM analysis with a magnification of A) 500 \times , B) 25 000 \times and C) 100 000 \times for Co^{II}Co^{III}-CO₃.

a quasi $\pi/2$ angle toward Z' axis underlining a behavior close to an ideal capacitor. A second constant phase element (CPE_d) was necessary to fit the lower frequency part where a change of slope in Z'' vs Z' curve is observed. Less abrupt than in the higher part, the phase constant is fixed at 0.5, corresponding to a $\pi/4$ angle with a real axis and representative of a diffusive Warburg-type process. Counterintuitively, well shaped CV peaks arising from redox reactions, even fast ones, should be observed with a Z'' - Z' (ω) frequency dependence, by a usual convex downward semi-circle, but they are absent here. It should be interpreted that redox reactions are occurring mostly at the surface, revealing no bulk effect (intra-granular interactions). Compared with the Co₂Al-CO₃ reference, the CPE_{et} values are multiplied by 30 for the Co^{II}Co^{III} samples. Contrary to CPE_{et}, the CPE_d is almost the same for all compounds, indicating a similar diffusion phenomenon.

2.3.3. Galvanostatic Charge and Discharge Study

Co^{II}Co^{III}-CO₃ reference presents a pseudo-capacitive behavior which is interesting for electrochemical applications as supercapacitors and more precisely as “pseudo-capacitors”. Capacitive performances of the as-prepared LDH thin film electrodes were scrutinized by Galvanostatic cycling in a 0.1 M KOH solution. The samples were allowed to perform over an optimized potential window using Galvanostatic cycling. The charge and discharge processes are shown in Figure 7C and D.

Applying current densities from 0.5 up to 50 A.g⁻¹ allowed us to obtain Ragone plots for the charge and discharge of the compounds, representing power density (W.kg⁻¹) vs energy density (W.h.kg⁻¹).^[32] At a current density of 0.5 A.g⁻¹, Co^{II}Co^{III}-CO₃ exhibits a capacity as high as 1490 F.g⁻¹, whereas the capacitance for Co₂Al-CO₃ is limited to 760 F.g⁻¹ (Table 4). At a higher current density of 50 A.g⁻¹, the monometallic LDH composition sustains 20 F.g⁻¹, but only 2 F.g⁻¹ for Co₂Al-CO₃, thus clearly demonstrating the significantly higher pure capacitive properties (response in short time) for Co^{II}Co^{III}-CO₃ compared to the Co₂Al-CO₃ reference LDH.

To the best of our knowledge, the obtained values are among the highest values ever reported for LDH compounds. It is also worth noting that the present electrode material is straightforwardly coated as a thin film onto the electrode surface, in the absence of any linking agent such as acetylene black or additives for enhancing electronic paths, like graphene,^[6,8,33] which would increase the response at shorter times.

The stability upon cycling (charge and discharge) was evaluated after 100 cycles at 1 A.g⁻¹ and 300 cycles at 2 A.g⁻¹ (Figure 8). The loss of capacity for Co^{II}Co^{III}-CO₃ was about 25% for charging at 1 A.g⁻¹ (Figure 8A) and 15% at 2 A.g⁻¹ (Figure 8B), whereas the electrochemical net balance between cathodic and anodic sweeps (efficiency), representing the ratio of charge/discharge capacities, is found to be stable upon cycling at around 37% at 1 A.g⁻¹ and 65% at 2 A.g⁻¹ (Figure 8A,B).

Typical Ragone plots of charge and discharge for Co^{II}Co^{III}-CO₃ (Figure 8C and D) exhibit features ranking them from capacitor to battery-type performances with an energy density of 340 mW.h.kg⁻¹ at a power density of 17.5 kW.kg⁻¹ and 25.4 W.h.kg⁻¹ at a power density of 175 W.kg⁻¹ for charge. The comparison can be made with Co₂Al-CO₃ LDH, which has an energy density of 32 mW.h.kg⁻¹ at a power density of 17.5 kW.kg⁻¹ and 12.4 W.h.kg⁻¹ at a power density of 175 W.kg⁻¹. Indeed, the difference between Co^{II}Co^{III}-CO₃ and Co₂Al-CO₃ of a factor 10 at low power density slightly levels out when increasing the power density, and such a behavior competes well with other systems containing nickel hydroxides and graphene^[34,35] or cobalt-containing materials like CoO even doped with carbon microspheres,^[36] cobalt hydroxide nanoflakes,^[37,38] cobalt hydroxide with CNTs,^[39] mesoporous Co₃O₄,^[40] or Ni-Co LDH nanosheets.^[41]

2.3.4. Characterization of Materials after Electrochemical Treatment

To further investigate the possible changes in both short-range and long-range structural order that occur during the electrochemical treatment of Co^{II}Co^{III}-CO₃, the atomic pair distribution

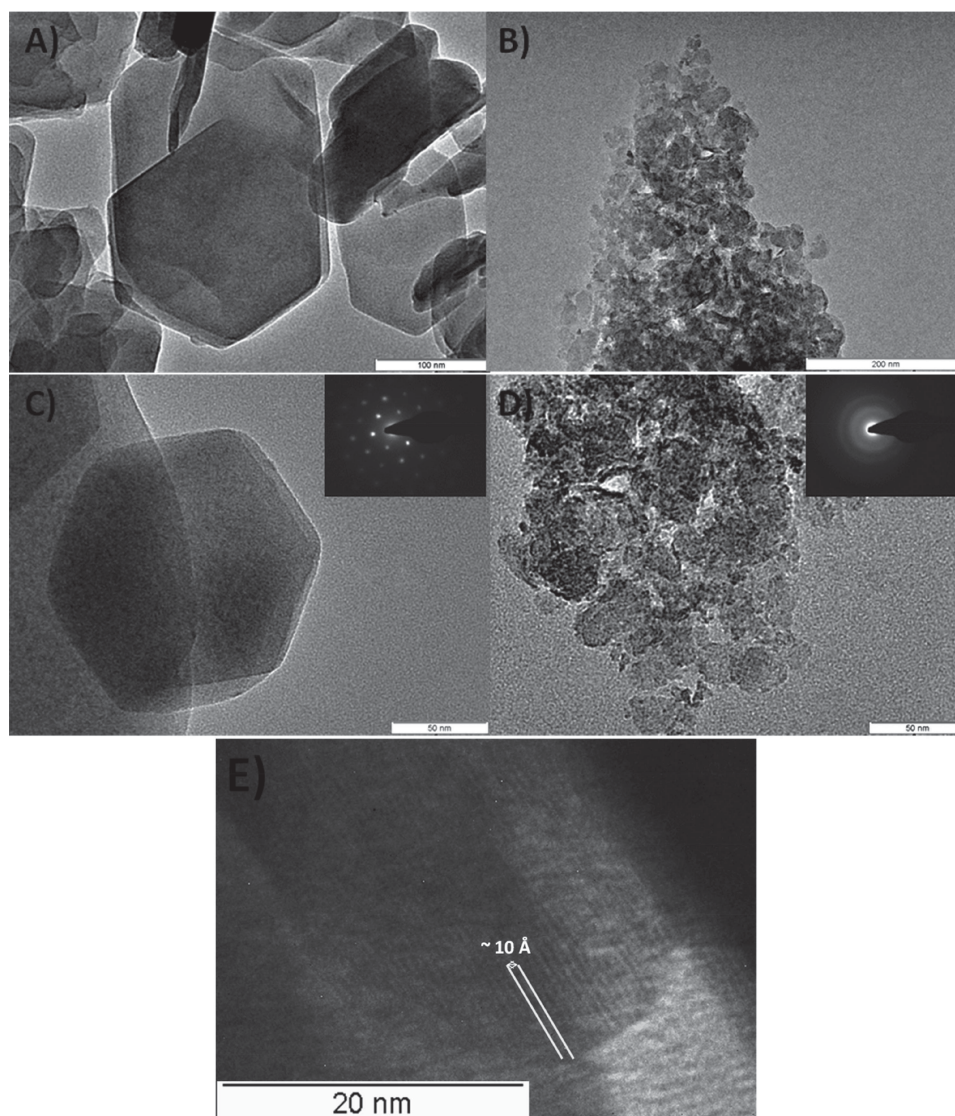


Figure 6. TEM analysis of A) $\text{Co}_2\text{Al-CO}_3$ and B) $\text{Co}^{\text{II/III}}\text{-CO}_3$ with a magnification of 57 000 \times and C,D) with magnification of 97 000 \times . Insets show electronic diffraction of the observed particles. E) Lamellar stacking observed with magnification of 230 000 \times .

Table 4. Charge and discharge capacities at different current densities.

| Current density [A.g ⁻¹] | $\text{Co}_2\text{Al-CO}_3$ | | | $\text{Co}^{\text{II/III}}\text{-CO}_3$ | | |
|---|---|--|---------------------|---|--|---------------------|
| | Charge Capacity [F.g ⁻¹] | Discharge Capacity [F.g ⁻¹] | Net balance* [%] | Charge Capacity [F.g ⁻¹] | Discharge Capacity [F.g ⁻¹] | Net balance* [%] |
| 0.5 | 720 | 265 | 36 | 1490 | 335 | 23 |
| 1 | 320 | 200 | 63 | 860 | 305 | 37 |
| 2 | 200 | 150 | 75 | 405 | 260 | 65 |
| 5 | 135 | 120 | 89 | 280 | 200 | 71 |
| 10 | 90 | 80 | 89 | 205 | 165 | 80 |
| 20 | 30 | 30 | 100 | 110 | 95 | 86 |
| 50 | 2 | 2 | 100 | 20 | 20 | 100 |

*Net capacitance balance between cathodic and anodic sweeps.

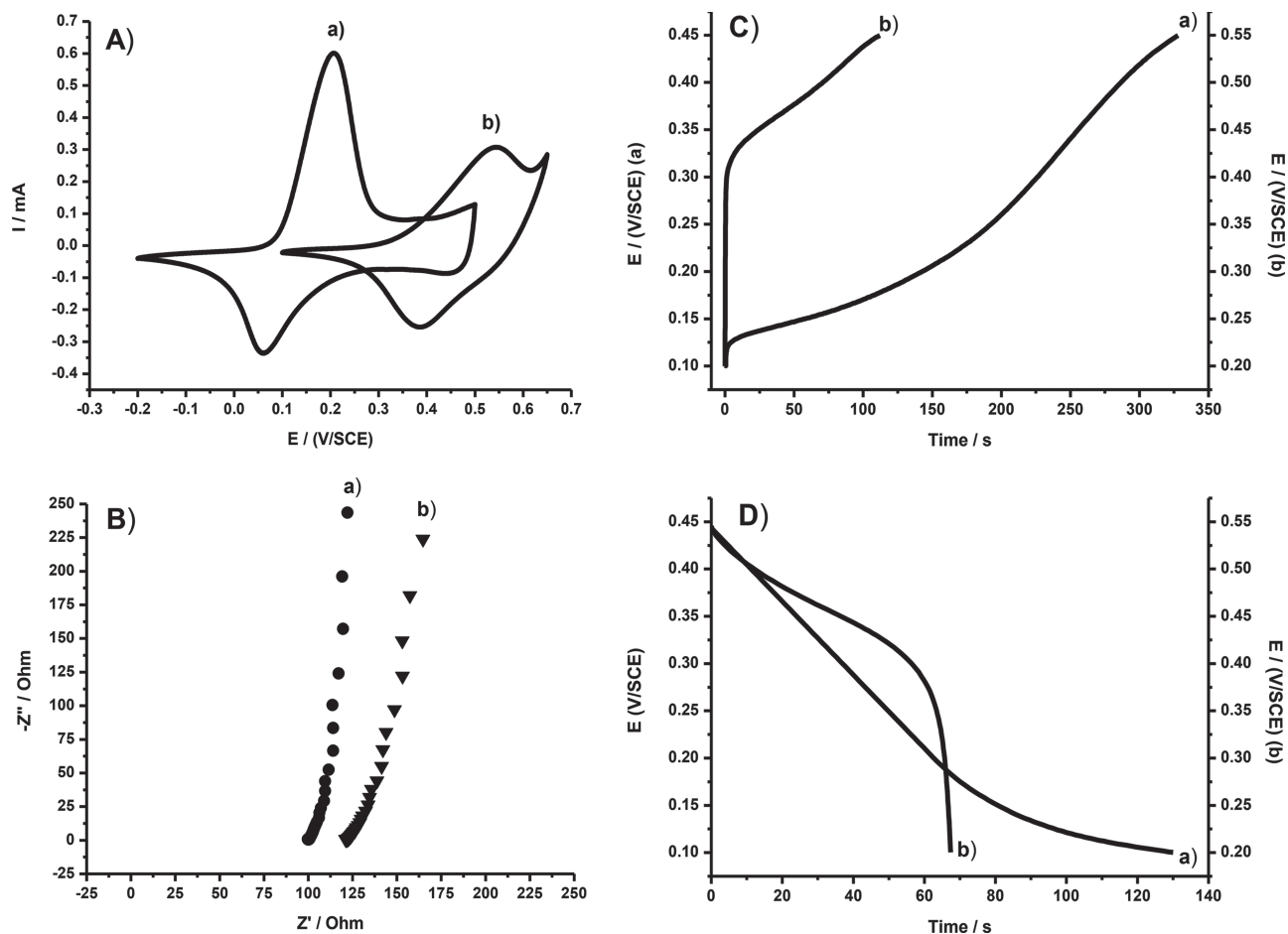


Figure 7. A) Cyclic voltammograms, B) EIS spectra, C) charge curves, and D) discharge curves for a) $\text{Co}^{\text{II}}\text{Co}^{\text{III}}\text{-CO}_3$ and b) $\text{Co}_2\text{Al-CO}_3$.

functions were also measured on two electrochemically treated samples: $\text{Co}^{\text{II}}\text{Co}^{\text{III}}\text{-CO}_{3\text{ox}}$, which was obtained after electrolysis at a potential of 0.45 V/SCE for 8 h, and $\text{Co}^{\text{II}}\text{Co}^{\text{III}}\text{-CO}_{3\text{ox/red}}$, which was oxidized for 8 h at a potential of 0.45 V/SCE then reduced for 8 h at a potential of 0 V/SCE. To better understand the origin of performance and discriminate between surface and bulk effects, as well as possibly explain the electrochemical efficiency deviating from 1 (in time and in power (Table 4), the composition of electrochemically treated samples was also determined using both iodometric titration and XPS. The values were compared with those obtained by PDF analysis (Table 2). As previously noticed, Co^{III} percentages determined by XPS appear systematically higher than with the other methods.

In Figure 4C, the experimental PDFs of the electrochemically-treated samples are compared to $\text{Co}^{\text{II}}\text{Co}^{\text{III}}\text{-CO}_3$ reference. As can be seen, the changes are many and concern at first the first peak of the PDF. This peak corresponds to the Co-O_{OH} distances within $\text{Co}^{\text{II}}/\text{Co}^{\text{III}}(\text{OH})_6$ octahedra and is sensitive to the $\text{Co}^{\text{II}}/\text{Co}^{\text{III}}$ ratio. For $\text{Co}^{\text{II}}\text{Co}^{\text{III}}\text{-CO}_{3\text{ox}}$ sample, the PDF peak broadens and almost splits in two peaks probably due to a more important contribution of $\text{Co}^{\text{III}}\text{-OH}$ bond lengths as a result of the oxidation process. The deconvolution of this peak by two Gaussians leads to two distances 1.89 Å and 2.15 Å attributed to $\text{Co}^{\text{II}}\text{-OH}$

and $\text{Co}^{\text{III}}\text{-OH}$ respectively (see 2.1). The relative percentages of Co^{II} and Co^{III} determined from peak areas are 46% Co^{II} and 54% Co^{III} (Figure 4Da). These values are in the same order as those obtained with iodometric titration and XPS analysis (Table 2).

By comparison, a narrower and more intense PDF peak is observed for $\text{Co}^{\text{II}}\text{Co}^{\text{III}}\text{-CO}_{3\text{ox/red}}$ as a consequence of the reduction process. Gaussian fitting gives two distances at 1.85 Å and 1.98 Å, attributed to $\text{Co}^{\text{II}}\text{-OH}$ and $\text{Co}^{\text{III}}\text{-OH}$, respectively. The relative percentages are 79% for Co^{II} and 21% for Co^{III} (Figure 4Db), which lie between the values obtained by XPS and iodometric titration (Table 2), reflecting the different scale of analysis and indicating a net difference in composition between surface and bulk, as suggested above. During XPS analysis, collected data associated to Figures 2B,C, have shown a clear evolution of the experimental profile in relation with the redox processes.

As expected, changes on the O_{OH} shell around $\text{Co}^{\text{II}}/\text{Co}^{\text{III}}$ atoms result in changes in the Co-Co distances at a , $\sqrt{3}a$, and $2a$, and these are rather important in the case of $\text{Co}^{\text{II}}\text{Co}^{\text{III}}\text{-CO}_{3\text{ox/red}}$ sample. We also have to consider a possible degradation of the material and the formation of phases such as Co_3O_4 , CoOOH and $\beta\text{Co}(\text{OH})_2$. In Figure 4E are compared the experimental PDFs of the electrochemically-treated samples with calculated PDF for $\beta\text{Co}(\text{OH})_2$, CoOOH and Co_3O_4 ;

although it is not easy to be affirmative, it seems that none of these latter phases is present.

3. Conclusions

TOR of $\beta\text{-Co}(\text{OH})_2$ yields a $\text{Co}^{\text{II}}\text{Co}^{\text{III}}\text{-CO}_3$ LDH-type material with a $\text{Co}^{\text{III}}/\text{Co}_{\text{tot}}$ ratio measured by chemical titration of about 0.13. The average oxidation state is in agreement with XPS and XANES measurements, and slightly over-estimated by EXAFS refinement of the first shell composed of two Co-O overlapped contributions. Similarly, both contributions are depicted by a PDF analysis, and their refinement accords well with the chemical analysis. The resulting electrochemical behavior was scrutinized along with the structural evolution occurring upon electrochemical treatment by coupling analysis techniques. It appeared that, after the electrochemical oxidation, the mean amount of Co^{III} present in the LDH layer increased from 13% to 60%. The net balance between half cycles, characteristic of the electrochemical efficiency, deviates from 1, resulting in an average value stabilized at 30% of Co^{III} after reduction. This results in the usual ratio of 2 to 1 between divalent and trivalent cations in the LDH composition. Finally, the sample $\text{Co}^{\text{II}}\text{Co}^{\text{III}}\text{-CO}_3$ is found to perform well at a high power density due to a

wettability of the electrolyte in association with a rapid surface redox reaction.

4. Experimental Section

4.1. Materials Synthesis

$\text{Co}(\text{NO}_3)_2 \cdot 6\text{H}_2\text{O}$ (Acros, 99%); NH_4OH (Acros, 28–30% wt. in water); and KOH (Sigma-Aldrich) were used as received without further purification. Deionized water was employed throughout all the experiments. Dry air was used for oxidation of Co^{II} cations.

$\text{Co}^{\text{II}}\text{Co}^{\text{III}}\text{-CO}_3$ compound was prepared by TOR, adapting the protocol described by Xu and Zeng,^[12,13] using O_2 contained in air as the oxidizing agent. Typically, 25 mL of 0.1 M $\text{Co}(\text{NO}_3)_2$ solution was quickly added to 250 mL of 0.5 M NH_4OH solution in the reactor just after air bubbling started. After stirring for 60 h at 40 °C, the solution was centrifuged at 4500 rpm for 10 min and was then rinsed three times with deionized water. The solid was finally dried in air at 30 °C overnight. $\text{Co}_2\text{Al-CO}_3$ was prepared with a $\text{Co}^{\text{II}}/\text{Al}$ ratio of 2 by a coprecipitation method as described previously.^[42,43]

4.2. Physical Characterization

The oxidation rate of Co^{II} to Co^{III} after TOR was evaluated by coupling TGA measurements with iodometric titration of Co^{III} , as reported by Xu and Zeng.^[13,44] In this method, the total Co content (Co_{tot}) was

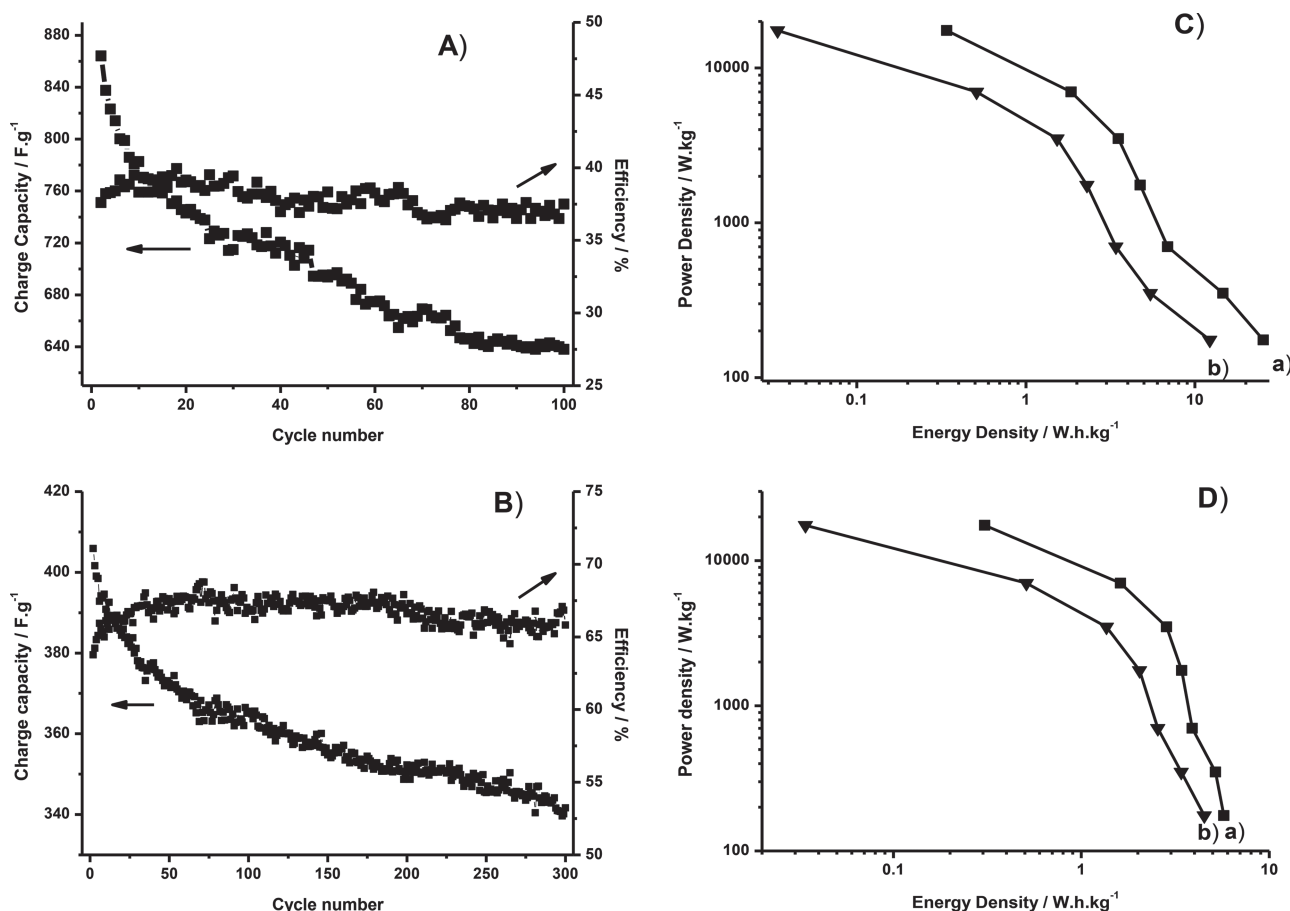


Figure 8. Charge capacity and electrochemical net balance (efficiency) evolution with cycle number at A) 1 A.g⁻¹ and B) 2 A.g⁻¹ for $\text{Co}^{\text{II}}\text{Co}^{\text{III}}\text{-CO}_3$. Ragone plot for C) charge and D) discharge of a) $\text{Co}^{\text{II}}\text{Co}^{\text{III}}\text{-CO}_3$ and b) $\text{Co}_2\text{Al-CO}_3$.

determined by using TGA analysis considering that only Co_3O_4 was obtained above 600 °C: this was confirmed by XRD analysis of the residual product. TGA analyses were made on a Setaram 92–16.16 under air flow in the temperature range 25–1100 °C with a linear temperature ramp of 5 °C per min. Iodometric titration of Co^{3+} content was realized with 20 mg of LDH phases dissolved in an acidified 0.1 M KI solution. The corresponding concentration of formed I_2 was determined by UV spectroscopy at 352 cm^{-1} ($\epsilon = 12\,000\text{ cm}^{-1}\cdot\text{L}^{-1}\cdot\text{mol}^{-1}$). The analysis was performed on a Nicolet Evolution 500 from Thermo Scientific between 200 and 500 cm^{-1} .

XPS measurements were performed on a Thermo K-alpha spectrometer with a hemispherical analyzer and a microfocussed (analysis area was ca. 400 μm^2) monochromatized radiation ($\text{AlK}\alpha$, 1486.6 eV) operating at 72 W under a residual pressure of 10^{-9} mbar. The pass energy was set to 20 eV. Charge effects were compensated for by the use of a dual beam charge neutralization system (low energy electrons and Ar^+ ions) which had the unique ability to provide consistent charge compensation. All the neutralizer parameters remained constant during analysis and allow ones to find a 285.0 eV C(1s) binding energy for adventitious carbon. Spectra were mathematically fitted with Casa XPS software using a least squares algorithm and a nonlinear baseline. The fitting peaks of the experimental curves were defined by a combination of Gaussian (70%) and Lorentzian (30%) distributions. Infrared spectra were recorded in transmission mode using the KBr pellet technique with a Nicolet 5700 spectrometer from Thermo Scientific over the wavenumber domain from 400 to 4000 cm^{-1} with a number of scans of 128 and a resolution of 4 cm^{-1} . The samples were diluted to about 20% weight with KBr.

SEM analyses were made using a Zeiss Supra 55 VP with an acceleration voltage of 3 kV with magnifications of 500 \times , 5000 \times and 50 000 \times . TEM images were taken on a Philips CM20 electron microscope operating at 200 kV; the LDH powders were suspended in ethanol overnight, and a drop of the suspension was deposited onto a 400 mesh holey carbon-coated copper grid and allowed to dry at room temperature.

Powder X-Ray Diffraction (PXRD) measurements were performed using a Siemens D501 diffractometer in Bragg-Brentano geometry with $\text{Cu-K}\alpha_1/\alpha_2$ radiation. Data were collected between 4.0 and 70.0 $2\theta^\circ$, with a step size of 0.08 $2\theta^\circ$ and a counting time of 3 s/step. Cell parameters were determined from profile refinement using the FULLPROF suite programs^[45] and considering the R-3m space group. The instrumental contribution to peak broadening was determined with Y_2O_3 standard. To treat anisotropic size effects, the Lorentzian part of the peak broadening was modeled with linear combinations of spherical harmonics which allow the calculation of the crystallite average size along each reciprocal lattice vector.^[17] Assuming disk-shaped crystallites, the apparent size for the 00l reflections corresponds to the thickness of the disk and the diameter is obtained from the apparent size for 110 reflections multiplied by $3\pi/8$.^[46]

The PDFs were obtained from high resolution powder X-ray diffraction data collected on the beamline CRISTAL at synchrotron Soleil (France). A monochromatic beam of wavelength 0.4388 Å was extracted from the undulator beam using a double crystal Si(111) monochromator. Each sample was loaded in a rotating 0.7 mm diameter glass capillary, which was mounted on a two circle diffractometer equipped with a 21 crystals multi-analyzer. The PDF method is based on the total scattering pattern, where the Bragg peaks and the diffuse component both reflect the average longer-range atomic structure and the local structural imperfections.^[47] At first, the diffraction pattern was corrected for background, which was determined using a separate diffraction measurement of an empty glass capillary, and taking into account Compton scattering, absorption, and polarization. All these corrections were done using the program PDFgetX2.^[48] Subsequently, the corrected X-ray diffraction data were scaled into electron units and the structure function $S(Q)$ was calculated. The PDF, which gives the probability to find an atom at a distance r away from another atom, was obtained by a Fourier transformation of $S(Q)$ according to Equation (1):

$$G(r) = \frac{2}{\pi} \int_0^\infty Q[S(Q) - 1] \sin Qr dQ \quad (1)$$

where Q is the magnitude of the scattering vector. $S(Q)$ was truncated at $Q_{\text{max}} = 25.4\text{ Å}^{-1}$, the signal-to-noise ratio being unfavorable beyond that value of Q . The simulated PDFs using structural data from the inorganic crystal structure database ICSD were compared to the experimental PDF using the software PDFFIT.^[49]

Co K-edge XAS spectra were collected at SUPERXAS Beamlines of SLS in the transmission mode at room temperature. The beam was monochromatized by a Si (111) double-crystal. The beam intensity was reduced by 30–40% to minimize the high-order harmonics. The XANES and EXAFS spectra were processed using Athena software package.^[50] For the XANES, the reference spectrum of a Co foil was collected simultaneously with the sample spectra for the energy calibration. For the analysis, a linear background was fitted to the pre-edge region and subtracted from the spectra which were normalized in a consistent way. Data were calibrated in energy using the maximum of the first derivative of the metallic Co foil at 7708.9 eV.

For the EXAFS analysis, a pre-edge background was removed using a linear function. A post-edge background using the Autobk algorithm was applied with a cutoff $\text{Rbkg} = 1$ and $k\text{-weight} = 3$ in order to isolate the EXAFS oscillations $\chi(k)$. The extracted EXAFS signal $\chi(k)$ was weighted by k^3 to emphasize the high-energy oscillations and then Fourier-transformed in a k range from 2.5 to 13 Å^{-1} using a Hanning window with a window (Δk) of 1.0 Å^{-1} , thereby obtaining magnitude plots of the EXAFS spectra in R-space. EXAFS fitting of distances and Debye-Waller factors was performed with the Artemis interface to IFEFFIT using least-squares refinements.^[51] The S_0^2 amplitude reduction parameter which takes multi-electronic effects into account and the energy shift E_0 were first calibrated by fitting relevant crystalline references, CoO , $\beta\text{-Co(OH)}_2$, $\text{Co}_2\text{Al(OH)}_3(\text{CO}_3)_{0.5} \cdot 2\text{H}_2\text{O}$, here called $\text{Co}_2\text{Al}-\text{CO}_3$ LDH and Co_3O_4 , which crystallize in Fm-3m (225), P-3m (164), R-3m (166) and Fd-3m (227) space group, respectively. The reliability of the fit was assessed by a residual factor that was minimized.

4.3. Electrochemical Characterization

Thin LDH films were used for electrochemical analysis. Typically, 10 μL of an overnight stirred 2 mg/mL LDH suspension (20 μg) were deposited on platinum electrodes. The Pt electrode surface was of 0.07 cm^2 . Before deposition, the electrode surface was polished with 1 μm diamond paste and washed with acetone and then polished again with 0.05 μm alumina slurry to be finally rinsed with water and ethanol. Cyclic Voltammetry, Galvanostatic Cycling and Electrochemical Impedance Spectroscopy measurements were made using a BioLogic Science Instruments SP-150. The experiments were made in a 0.1 M KOH solutions using a three-electrode cell, including a saturated calomel electrode (SCE) as reference electrode, a platinum auxiliary electrode and the platinum electrode coated with LDH thin films as working electrode. Nyquist plots were then fitted with ZView software to determine equivalent circuits. For the latter and for a reason of simplicity, three components were used: an ohmic resistance for the electrolyte resistance, and two constant phase elements (CPE) CPE_{et} and CPE_d associated to an impedance $1/(j\omega)^n$, where j is an imaginary number, C is the capacitance of the CPE and n represent the deviation from a pure capacitor ($n = 1$).

Galvanostatic Cycling with Potential Limitation were duplicated over a potential window from 0 to 0.45 V/SCE for charge experiments and from 0.45 to 0 V/SCE for discharge experiments. The current densities employed were 0.5, 1.0, 2.0, 5.0, 10.0, 20.0, and 50.0 $\text{A}\cdot\text{g}^{-1}$. The current was so adjusted for a quantity of 20 μg of active LDH deposit on the platinum electrode. The capacity in charge and discharge was calculated using the formula:

$$C = \frac{I \cdot \Delta t}{m \cdot \Delta V} \quad (2)$$

Ragone charts were plotted calculating power density and energy density according to the formulas:

$$E = \frac{\Delta V \cdot I \cdot \Delta t}{m} \text{ and } P = \frac{\Delta V \cdot I}{m} \quad (3)$$

Reversibility was tested after cycling at 0.5 A.g⁻¹ after cycling at 50 A.g⁻¹ and cycling stability was checked doing 100 cycles at 1 A.g⁻¹ and 300 cycles at 2 A.g⁻¹.

Electrolyses at constant potential were finally carried out to oxidize and reduce the Co^{II} sites in the Co^{II}Co^{III}-CO₃. To this, 2 × 100 mg of Co^{II}Co^{III}-CO₃ powder were separately suspended into 0.1 M KOH solution and oxidized for 8 h at a potential of 0.45 V/SCE under stirring. For the first one and treated by oxidation at 0.45 V/SCE and reduced for 8 h at 0.0 V/SCE for the second sample. The solids were finally recovered by centrifugation and once dried, the evolution of the Co^{III}/Co_{tot} ratio was determined by XPS and PDF analysis.

Supporting Information

Supporting Information is available from the Wiley Online Library or from the author.

Acknowledgements

The authors would like to thank Guillaume Monier for TEM analysis and technical support from Nachtegaal Maarten beamline. The authors would like also to thank the funding "Cellule Energie INSIS".

Received: January 28, 2014

Revised: March 10, 2014

Published online: May 7, 2014

- [1] S. Chen, W. Xing, J. Duan, X. Hu, S. Z. Qiao, *J. Mater. Chem. A* **2013**, *1*, 2941.
- [2] H. Li, L. Deng, G. Zhu, L. Kang, Z.-H. Liu, *Mater. Sci. Eng. B* **2012**, *177*, 8.
- [3] Z. Fan, J. Yan, T. Wei, L. Zhi, G. Ning, T. Li, F. Wei, *Adv. Funct. Mater.* **2011**, *21*, 2366.
- [4] X.-M. Liu, Y.-H. Zhang, X.-G. Zhang, S.-Y. Fu, *Electrochim. Acta* **2004**, *49*, 3137.
- [5] Y. Wang, W. Yang, C. Chen, D. G. Evans, *J. Power Sources* **2008**, *184*, 682.
- [6] S. Huang, G.-N. Zhu, C. Zhang, W. W. Tjiu, Y.-Y. Xia, T. Liu, *ACS Appl. Mater. Interfaces* **2012**, *4*, 2242.
- [7] L. Zhang, X. Zhang, L. Shen, B. Gao, L. Hao, X. Lu, F. Zhang, B. Ding, C. Yuan, *J. Power Sources* **2012**, *199*, 395.
- [8] J. Fang, M. Li, Q. Li, W. Zhang, Q. Shou, F. Liu, X. Zhang, J. Cheng, *Electrochim. Acta* **2012**, *85*, 248.
- [9] L. Wang, D. Wang, X. Y. Dong, Z. J. Zhang, X. F. Pei, X. J. Chen, B. Chen, J. Jin, *Chem. Commun.* **2011**, *47*, 3556.
- [10] R. Ma, K. Takada, K. Fukuda, N. Iyi, Y. Bando, T. Sasaki, *Angew. Chem. Int. Ed.* **2008**, *47*, 86.
- [11] J. T. Sampanthar, H. C. Zeng, *Chem. Mater.* **2001**, *13*, 4722.
- [12] Z. P. Xu, H. C. Zeng, *Chem. Mater.* **2000**, *12*, 2597.
- [13] Z. P. Xu, H. C. Zeng, *Int. J. Inorg. Mater.* **2000**, *2*, 187.
- [14] A. Faour, C. Mousty, V. Prevot, B. Devouard, A. De Roy, P. Bordet, E. Elkaim, C. Taviot-Gueho, *J. Phys. Chem. C* **2012**, *116*, 15646.
- [15] *Order–Disorder in Clay Mineral Structure* (Ed: G. W. Brindley), Mineralogical Society, London **1980**.
- [16] A. Vaccari, *Appl. Clay Sci.* **2002**, *22*, 75.
- [17] M. Jarvinen, *J. Appl. Cryst.* **1993**, *26*, 525.
- [18] M. C. Richardson, P. S. Braterman, *J. Phys. Chem. C* **2007**, *111*, 4209.
- [19] J. Wong, F. W. Lytle, R. P. Messmer, D. H. Maylotte, *Phys. Rev. B: Condens. Matter* **1984**, *30*, 5596.
- [20] W.-S. Yoon, K.-B. Kim, M.-G. Kim, M.-K. Lee, H.-J. Shin, J.-M. Lee, J.-S. Lee, C.-H. Yo, *J. Phys. Chem. B* **2002**, *106*, 2526.
- [21] R. Ma, Z. Liu, K. Takada, K. Fukuda, Y. Ebina, Y. Bando, T. Sasaki, *Inorg. Chem.* **2006**, *45*, 3964.
- [22] N. E. Brese, M. O'Keeffe, *Acta Cryst. B* **1991**, *47*, 192.
- [23] F. Leroux, E. M. Moujahid, C. Taviot-Gueho, J.-P. Besse, *Solid State Sci.* **2001**, *3*, 81.
- [24] C. Mockenhaupt, T. Zeiske, H. D. Lutz, *J. Mol. Struct.* **1998**, *443*, 191.
- [25] S. J. Skinner, G. Amow, *J. Solid State Chem.* **2007**, *180*, 1977.
- [26] W. L. Smith, A. D. Hobson, *Acta Cryst. B* **1973**, *29*, 362.
- [27] A. Rujiwatra, C. J. Kepert, J. B. Claridge, M. J. Rosseinsky, H. Kumagai, M. Kurmoo, *J. Am. Chem. Soc.* **2001**, *123*, 10584.
- [28] Z.-L. Huang, M. Drillon, N. Masciocchi, A. Sironi, J.-T. Zhao, P. Rabu, P. Panissod, *Chem. Mater.* **2000**, *12*, 2805.
- [29] M. Shizuya, M. Isobe, E. Takayama-Muromachi, *J. Solid State Chem.* **2007**, *180*, 2550.
- [30] H. J. Orman, P. J. Wiseman, *Acta Cryst. C* **1984**, *40*, 12.
- [31] L. Aimoz, C. Taviot-Gueho, S. V. Churakov, M. Chukalina, R. Dähn, E. Curti, P. Bordet, M. Vespa, *J. Phys. Chem. C* **2012**, *116*, 5460.
- [32] D. Ragone, *SAE Technical Paper* **1968**, 680453.
- [33] C. Liu, Z. Yu, D. Neff, A. Zhamu, B. Z. Jang, *Nano Lett.* **2010**, *10*, 4863.
- [34] J. Yan, Z. Fan, W. Sun, G. Ning, T. Wei, Q. Zhang, R. Zhang, L. Zhi, F. Wei, *Adv. Funct. Mater.* **2012**, *22*, 2632.
- [35] Z. Tang, C.-h. Tang, H. Gong, *Adv. Funct. Mater.* **2012**, *22*, 1272.
- [36] Z.-C. Yang, C.-H. Tang, Y. Zhang, H. Gong, X. Li, J. Wang, *Sci. Rep.* **2013**, *3*.
- [37] L.-B. Kong, M. Liu, J.-W. Lang, Y.-C. Luo, L. Kang, *J. Electrochem. Soc.* **2009**, *156*, A1000.
- [38] A. D. Jagdale, V. S. Kumbhar, D. S. Dhawale, C. D. Lokhande, *Electrochim. Acta* **2013**, *98*, 32.
- [39] C.-H. Chen, D.-S. Tsai, W.-H. Chung, K.-Y. Lee, Y.-M. Chen, Y.-S. Huang, *J. Power Sources* **2012**, *205*, 510.
- [40] R. B. Rakhi, W. Chen, D. Cha, H. N. Alshareef, *Nano Lett.* **2012**, *12*, 2559.
- [41] H. Chen, L. Hu, M. Chen, Y. Yan, L. Wu, *Adv. Funct. Mater.* **2014**, *24*, 934.
- [42] S. Miyata, *Clays Clay Miner.* **1975**, *23*, 369.
- [43] P. Vialat, F. Leroux, C. Taviot-Gueho, G. Villemure, C. Mousty, *Electrochim. Acta* **2013**, *107*, 599.
- [44] Z. P. Xu, H. C. Zeng, *Chem. Mater.* **2000**, *12*, 3459.
- [45] C. Rodriguez-Carvajal, *J. Powder Diffr.* **2001**, Newsletter, 12.
- [46] J. I. Langford, D. Louer, *J. Appl. Cryst.* **1982**, *15*, 20.
- [47] S. J. L. Billinge, *J. Solid State Chem.* **2008**, *181*, 1695.
- [48] X. Qiu, J. W. Thompson, S. J. L. Billinge, *J. Appl. Cryst.* **2004**, *37*, 678.
- [49] T. Proffen, S. J. L. Billinge, *J. Appl. Cryst.* **1999**, *32*, 572.
- [50] B. Ravel, M. Newville, *J. Synchrotron Radiat.* **2005**, *12*, 537.
- [51] M. Newville, *J. Synchrotron Radiat.* **2001**, *8*, 322.